# Ab initio study of energy loss and wake potential in the vicinity of a graphene monolayer

**Despoja, Vito; Dekanić, Krešimir; Šunjić, Marijan; Marušić, Leonardo**

*Source / Izvornik:* **Physical review B: Condensed matter and materials physics, 2012, 86**

**Journal article, Published version**
**Rad u časopisu, Objavljena verzija rada (izdavačev PDF)**

https://doi.org/10.1103/PhysRevB.86.165419

*Permanent link / Trajna poveznica:* https://urn.nsk.hr/urn:nbn:hr:217:931364

# *Ab initio* study of energy loss and wake potential in the vicinity of a graphene monolayer

V. Despoja,[1,2,3,*] K. Dekanić,[2,†] M Šunjić,[1,2,‡] and L. Marušić[4,§]

[1]*Donostia International Physics Center (DIPC), P. Manuel de Lardizabal 4, 20018 San Sebastian, Basque Country, Spain*

[2]*Department of Physics, University of Zagreb, Bijenička 32, HR-10000 Zagreb, Croatia*

[3]*Universidad del Pais Vasco, Centro de Fisica de Materiales CSIC-UPV/EHU-MPC, Avenida de Tolosa 72, E-20018 San Sebastian, Spain*

[4]*Maritime Department, University of Zadar, M. Pavlinovića b.b., HR-23000 Zadar, Croatia*

(Received 27 June 2012; published 11 October 2012)

A propagator of the dynamically screened Coulomb interaction in the vicinity of a graphene monolayer is calculated using ground-state Kohn-Sham orbitals, and the imaginary part of this propagator is used to calculate the energy-loss rate of a static blinking point charge due to excitation of electronic modes in graphene. Energy loss calculated for all $(Q,\omega)$ modes gives intensities of electronic excitations, including plasmon dispersions in graphene, with low-energy two-dimensional (2D) and high-energy $\pi_1$, $\pi_2$, and $\pi+\sigma$ plasmons. Plasmon energies are in good agreement with experimental results. This spectral analysis also enables us to study the contribution of each plasmon mode to the stopping power and potential induced by a point charge moving parallel to the graphene. We find the bow waves that in pristine graphene appear for higher velocities ($v \geqslant 2v_F$) and predominantly originate from excitation of $\pi$ plasmons. Doping induces extra features which appear for lower $v \approx v_F$ velocities and predominantly originate from the excitation of 2D or Drude plasmons.

DOI: 10.1103/PhysRevB.86.165419 PACS number(s): 73.22.Pr, 71.45.Gm

## I. INTRODUCTION

Graphene is a material with a very simple structure consisting of carbon atoms arranged in a honeycomb lattice,[1–4] and at the same time it is a very strong material that can be easily synthesized.[5–7] This makes graphene very interesting for many practical applications. For example, graphene monolayers or bilayers could become superior to noble metals in photonics[8] or plasmonics[9,10] and could be a material suitable for nanoelectronics.[11] Also, since plasmon resonance in a two-dimensional structure produces enhanced near-field effects similar to those at noble metal surfaces, it becomes interesting in plasmon-enhanced nanosensing[12] or in heat transfer processes.[13]

Proper understanding of such applications requires accurate experimental and theoretical studies of single-particle and collective excitations in graphene. For many applications it is very important to understand the mechanisms affecting the lifetime or propagation length of plasmons, which are subject to various decay mechanisms such as the creation of electron-hole pairs, phonons, etc.[9] Even though there have been many theoretical[14–16] and experimental[16–19] studies of various plasmon excitations in graphene, there is still a lack of proper theoretical description of plasmon decay mechanisms. Also, for many applications it is very important to understand the most appropriate way to design external longitudinal (dynamical charge distribution) or transverse (electromagnetic wave) probes able to excite plasmons in graphene selectively and efficiently.

In this paper we focus on the investigation of efficiency and selectivity of the simplest longitudinal probes, static blinking point charge and the moving point charge, in exciting various plasmons in pristine and doped graphene. Similar calculations have been done using a simple dielectric model,[20] where only excitation of a low-energy two-dimensional (2D) plasmon was considered, or by using the hydrodynamic model,[21] where the wake potential in carbon nanotubes has been investigated. Here we are in the framework of more general theories established a long time ago to investigate the energy loss and wake potential of moving ions close to a solid surface[22] or the wake potential and self-energy of a particle moving near a metallic surface[23,24] by using simple plasmon-pole or semiclassical approximations.[25]

In this work the response function and the induced potential are obtained using the first-principles time-dependent density functional theory (TDDFT) to calculate the dynamical response function and the energy-loss rate, where we include contributions of all electronic excitations up to 25 eV. Using the response function, we calculate the propagator of the dynamically screened Coulomb interaction and then use the imaginary part to obtain the energy-loss rate of a static blinking point charge in the vicinity of graphene. By scanning the energy dissipation across all $(Q,\omega)$ modes, we obtain the map of electron-hole and plasmon excitations in pristine and doped graphene. For energies of $\pi$ and $\pi+\sigma$ plasmons at the $\Gamma$ point, we get 4.5 and 14.3 eV, respectively, which is in good agreement with the reported experimental values of 4.7 and 14.6 eV,[16] or 5.1 and 14.5 eV,[18] as well as with recent theoretical results.[15,26] The dispersion curve of the low-energy 2D plasmon is not in a good agreement with the one obtained from simple one-band 2D theory but it is in a good agreement with previous more accurate theoretical[14,15] and experimental[17] results. In our opinion, this happens because simple one-band 2D electron gas theory is not sufficient for realistic and accurate description of low-energy 2D plasmons. We also obtain the splitting of $\pi$ plasmon for higher-momentum-transfer vectors, which has been observed experimentally.[19,27] In accordance with this, we introduce notation $\pi_1$ for a high-energy dispersive $\pi$ plasmon, and $\pi_2$ for a low-energy nondispersive plasmon.

We used the imaginary part of the induced dynamically screened Coulomb interaction $\mathrm{Im}W^{\mathrm{ind}}_{\mathbf{G}}(\mathbf{Q},\omega,z,z')$ to calculate stopping power and the real part $\mathrm{Re}W^{\mathrm{ind}}_{\mathbf{G}}(\mathbf{Q},\omega,z,z')$ to calculate the potential induced by a point charge moving parallel to the graphene surface. For the velocity unit we used the Fermi

 

velocity in the metal with density corresponding to $r_s = 3$ (in International System units this is $v_F = 1.4 \times 10^6$ m/s). We show that in pristine graphene and for velocities $v > 2v_F$ a moving particle produces waves of induced potential lagging behind the particle (bow waves). We demonstrate that these waves come from the excitation of $\pi_1$ plasmons. In doped graphene the bow wave appears for lower velocities $v \approx v_F$ as a consequence of excitation of low-energy 2D plasmons. We show that a broad $\pi + \sigma$ plasmon does not contribute significantly to the induced potential.

In Sec. II we describe the first-principles (DFT) method (which uses periodically repeated supercells in the $z$ direction), from which we obtain the Kohn-Sham (KS) orbitals in graphene. Then we describe how to use the KS orbitals in the calculation of the free-electron response function $\chi^0(z,z')$. Limiting $\chi^0(z,z)$ to a single unit supercell, e.g., $-L/2 < z,z' < L/2$, and using a bare Coulomb propagator, we construct the random phase approximation (RPA)-Dyson equation for the interacting electron response function $\chi(z,z')$, which does not include interaction with the neighboring supercells. In Sec. III we calculate the propagator of the dynamically screened Coulomb interaction and use its imaginary part to obtain the energy-loss rate of a static blinking point charge in the vicinity of graphene. By scanning the energy dissipation across the $(Q,\omega)$ space we obtain a map of plasmon modes in pristine and doped graphene. In Sec. IV we use the imaginary part of the dynamically screened Coulomb interaction propagator to calculate the stopping power of a charged particle moving parallel to the graphene monolayer, and in Sec. V we use its real part to calculate the potential induced by a charged particle moving parallel to the graphene monolayer. We analyze how the features in the stopping power and induced potential depend on the particle velocity. In Sec. VI we present conclusions.

## II. THEORY AND COMPUTATIONAL METHODS

### A. Ground-state calculation

In this section we briefly describe the calculation of the KS wave functions and energy levels (band structure) in a graphene monolayer that are used to calculate the independent electron response function. A schematic representation of a graphene monolayer is shown in Fig. 1. For electronic structure calculations we used a plane-wave self-consistent field DFT code (PWSCF) within the QUANTUM ESPRESSO (QE)

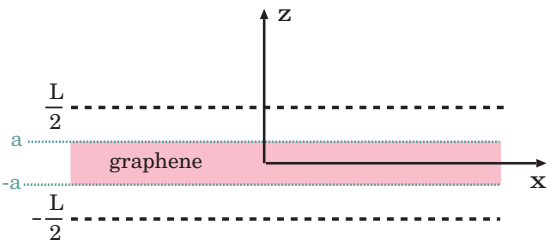


FIG. 1. (Color online) Schematic representation of the graphene monolayer. Unit cell parameter in the parallel direction is $a = 4.651$ a.u., in the perpendicular direction is $L = 5a$, and the thickness of the electronic density is $2a$.

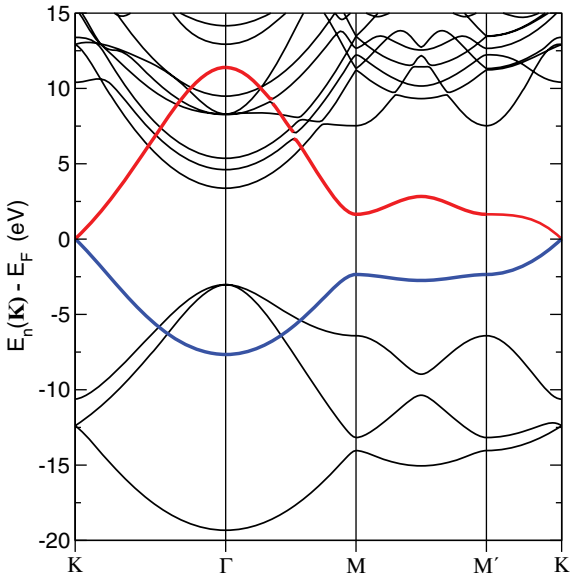


FIG. 2. (Color online) Graphene band structure. Blue line shows occupied $\pi$ band and red line shows unoccupied $\pi^*$ band.

package,[28] and the Perdew-Zunger local density approximation (LDA) for the exchange correlation (XC) potential.[29] An electronic temperature of $k_B T \approx 0.1$ eV was assumed to achieve convergence in the calculation of the KS wave functions, and all energies were then extrapolated to 0 K. The ground-state electronic density was calculated using a $12 \times 12 \times 1$ Monkhorst-Pack special $K$-point mesh, i.e., by using 19 special points in the irreducible Brillouin zone. In the PWSCF code we used norm-conserving LDA-based pseudopotentials for carbon atoms,[30] and we found the energy spectrum to be convergent with a 50-Ry plane-wave cutoff. Graphene band structure along the high-symmetry $\Gamma$-$K$-$M$-$\Gamma$ direction shown in Fig. 2 was calculated along the path with 241 $k$ points, and it agrees with previous calculations.[31] For the graphene unit cell parameter we used the experimental value $a = 4.651$ a.u. and for the unit cell in the $z$ direction, which represents separation between periodically repeated graphene layers, we take $L = 5a = 23.255$ a.u. (to ensure that the interlayer electronic densities do not overlap), as is shown in Fig. 1. For the response function it is important to choose the right thickness of the electron density, which we here take to be $2a$, as shown in Fig. 1.

### B. Response function calculation

The independent electron response function matrix can be written as

$$\chi^0_{\mathbf{G}\mathbf{G}'}(\mathbf{Q},\omega) = \frac{2}{V} \sum_{\mathbf{K}\in S.B.Z.} \sum_{n,m} \frac{f_n(\mathbf{K}) - f_m(\mathbf{K}+\mathbf{Q})}{\omega + i\eta + E_n(\mathbf{K}) - E_m(\mathbf{K}+\mathbf{Q})} \times M_{n\mathbf{K},m\mathbf{K}+\mathbf{Q}}(\mathbf{G})\, M^*_{n\mathbf{K},m\mathbf{K}+\mathbf{Q}}(\mathbf{G}'), \quad (1)$$

where $V = S * L$ is the normalization volume and $S$ is the normalization surface. In the summation over $\mathbf{K}$ we have used $101 \times 101 \times 1$ $K$-point mesh sampling, which corresponds to 10 303 Monkhorst-Pack special $k$ points in the Brillouin zone and 901 in the irreducible Brillouin zone. Also, $n,m$ summation is carried out over 50 bands, which proved to be

enough for the proper description of the high-energy $\pi + \sigma$ plasmon. Matrix elements in Eq. (1) have the form

$$M_{n\mathbf{K},m\mathbf{K}+\mathbf{Q}}(\mathbf{G}) = \langle \Phi_{n\mathbf{K}} | e^{-i(\mathbf{Q}+\mathbf{G})\mathbf{r}} | \Phi_{n\mathbf{K}+\mathbf{Q}} \rangle_V, \tag{2}$$

where $\mathbf{Q}$ is the momentum transfer vector parallel to the $x$-$y$ plane, $\mathbf{G} = (\mathbf{G}_\parallel, G_z)$ are three-dimensional (3D) reciprocal lattice vectors, and $\mathbf{r} = (\boldsymbol{\rho}, z)$ is a 3D position vector. Integration is performed over the normalization volume $V$. Plane-wave expansion of the wave function has the form

$$\Phi_{n\mathbf{K}}(\boldsymbol{\rho}, z) = \frac{1}{\sqrt{V}} e^{i\mathbf{K}\boldsymbol{\rho}} \sum_{\mathbf{G}} C_{n\mathbf{K}}(\mathbf{G}) e^{i\mathbf{G}\mathbf{r}},$$

where the coefficients $C_{n\mathbf{K}}$ are obtained by solving the KS equations. For energy cutoff in the wave function expansion we used 50 Ry, which corresponds to about 2500 $\mathbf{G}$ components. The free-electron response function (1) can be Fourier transformed in the $z,z'$ direction,

$$\chi^0_{\mathbf{G}_\parallel \mathbf{G}'_\parallel}(\mathbf{Q},\omega,z,z') = \sum_{G_z G'_z} \chi^0_{\mathbf{G}\mathbf{G}'}(\mathbf{Q},\omega) e^{iG_z z - iG'_z z'}, \tag{3}$$

which is a periodic function in the $z,z'$ direction, just as, e.g., LDA self-consistent electronic density, which follows periodically repeated graphene layers. Such behavior is schematically shown in Fig. 3. We are interested in the polarizability of electrons placed in just one of the periodically repeated samples, e.g., electrons located between $-L/2$ and $L/2$, as shown in Fig. 3. Since $\chi^0$ represents the polarizability of noninteracting electrons with nonoverlapping densities in different layers, the response function $\chi^0$ restricted to the interval $-L/2 < z,z' < L/2$ describes the polarizability of electrons in the corresponding graphene layer, without any influence from, or interaction with, electrons in surrounding graphene layers. In other words, contribution to the induced potential produced by a test charge placed at any position $z$ coming from polarization of electrons placed in the interval $-L/2 < z,z' < L/2$ without any influence of electrons in the rest of the system can be calculated by using the expression

$$W^{\mathrm{ind}}_{\mathbf{G}_\parallel}(\mathbf{Q},\omega,z,z') = \int_{-L/2}^{L/2} dz_1 dz_2\, v^{\mathrm{2D}}_{\mathbf{G}_\parallel}(\mathbf{Q},z,z_1)\, \chi^0_{\mathbf{G}_\parallel 0}(\mathbf{Q},\omega,z_1,z_2) \times v^{\mathrm{2D}}_0(\mathbf{Q},z_2,z'), \tag{4}$$

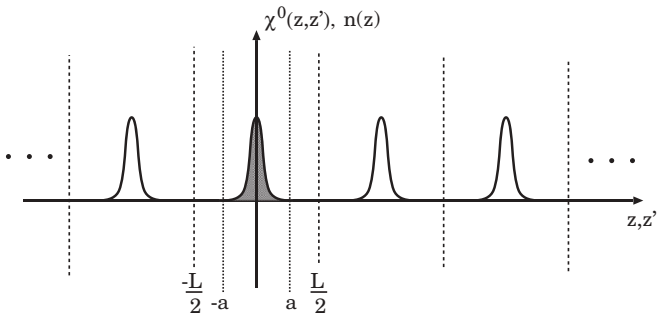


FIG. 3. Schematic representation of independent electron response function or LDA ground-state electronic density in periodically repeated graphene layers.

where $v^{\mathrm{2D}}_{\mathbf{G}_\parallel}(\mathbf{Q},z,z') = \frac{2\pi}{|\mathbf{Q}+\mathbf{G}_\parallel|} e^{-Q|z-z'|}$ is a 2D Fourier transform of the bare Coulomb interaction. In order to take into account the electron-electron interaction we need to replace the free-electron response function $\chi^0_{\mathbf{G}_\parallel \mathbf{G}'_\parallel}$ by the intralayer RPA response function $\chi_{\mathbf{G}_\parallel \mathbf{G}'_\parallel}$ obtained as the solution of the Dyson equation

$$\chi_{\mathbf{G}_\parallel \mathbf{G}'_\parallel}(\mathbf{Q},\omega,z,z') = \chi^0_{\mathbf{G}_\parallel \mathbf{G}'_\parallel}(\mathbf{Q},\omega,z,z') + \sum_{\mathbf{G}_{\parallel 1}} \int_{-L/2}^{L/2} dz_1 dz_2 \times \chi^0_{\mathbf{G}_\parallel \mathbf{G}_{\parallel 1}}(\mathbf{Q},\omega,z,z_1)\, v^{\mathrm{2D}}_{\mathbf{G}_{\parallel 1}}(\mathbf{Q},z_1,z_2) \times \chi_{\mathbf{G}_{\parallel 1},\mathbf{G}'_\parallel}(\mathbf{Q},\omega,z_2,z'). \tag{5}$$

Since integrations in Eq. (5) are performed from $-L/2$ to $L/2$, the density fluctuation created in the corresponding graphene layer (completely independent of other layers!) can, via Coulomb propagator $v^{\mathrm{2D}}_{\mathbf{G}_{\parallel 1}}(\mathbf{Q},z_1,z_2)$, interact only with density fluctuation in the same layer, and interaction with polarization in surrounding layers is completely excluded. This means from this point on that our calculation is actually performed for a single graphene layer, and it does not depend on the choice of $L$, assuming that $L$ is large enough to avoid the overlap of the electron orbitals in adjacent layers.

Using Fourier expansion (3), and a similar one for $\chi$, Dyson equation (5) becomes a matrix equation:

$$\chi_{\mathbf{G}\mathbf{G}'}(\mathbf{Q},\omega) = \chi^0_{\mathbf{G}\mathbf{G}'}(\mathbf{Q},\omega) + \sum_{\mathbf{G}_1\mathbf{G}_2} \chi^0_{\mathbf{G}\mathbf{G}_1}(\mathbf{Q},\omega)\, V_{\mathbf{G}_1\mathbf{G}_2}(\mathbf{Q}) \times \chi_{\mathbf{G}_2\mathbf{G}'}(\mathbf{Q},\omega), \tag{6}$$

where the Coulomb interaction matrix elements have the explicit form

$$V_{\mathbf{G}_1\mathbf{G}_2}(\mathbf{Q}) = \frac{4\pi}{|\mathbf{Q}+\mathbf{G}_1|^2}\delta_{\mathbf{G}_1\mathbf{G}_2} - p_{G_{z1}} p_{G_{z2}} \frac{4\pi(1-e^{-|\mathbf{Q}+\mathbf{G}_{\parallel 1}|L})}{|\mathbf{Q}+\mathbf{G}_{\parallel 1}|L} \times \frac{|\mathbf{Q}+\mathbf{G}_{\parallel 1}|^2 - G_{z1}G_{z2}}{\left(|\mathbf{Q}+\mathbf{G}_{\parallel 1}|^2 + G^2_{z1}\right)\left(|\mathbf{Q}+\mathbf{G}_{\parallel 1}|^2 + G^2_{z2}\right)} \delta_{\mathbf{G}_{\parallel 1}\mathbf{G}_{\parallel 2}} \tag{7}$$

with

$$p_{G_z} = \begin{cases} 1; & G_z = \frac{2k\pi}{L} \\ -1; & G_z = \frac{(2k+1)\pi}{L}, \end{cases} \quad k = 0,1,2,3,\ldots.$$

Solution of Eq. (6) has the form

$$\chi_{\mathbf{G}\mathbf{G}'}(\mathbf{Q},\omega) = \sum_{\mathbf{G}_1} \mathcal{E}^{-1}_{\mathbf{G}\mathbf{G}_1}(\mathbf{Q},\omega)\chi^0_{\mathbf{G}_1\mathbf{G}'}(\mathbf{Q},\omega), \tag{8}$$

where we have introduced the dielectric matrix

$$\mathcal{E}_{\mathbf{G}\mathbf{G}'}(\mathbf{Q},\omega) = \delta_{\mathbf{G}\mathbf{G}'} - \sum_{\mathbf{G}_1} V_{\mathbf{G}\mathbf{G}_1}(\mathbf{Q})\chi^0_{\mathbf{G}_1\mathbf{G}'}(\mathbf{Q},\omega). \tag{9}$$

Using Eqs. (3) and (4) (where $\chi^0_{\mathbf{G}_\parallel \mathbf{G}'_\parallel}$ should be replaced by $\chi_{\mathbf{G}_\parallel \mathbf{G}'_\parallel}$), the propagator of the induced dynamically screened Coulomb interaction can be written in terms of the matrix elements (8) (Ref. 32):

$$W^{\mathrm{ind}}_{\mathbf{G}_\parallel}(\mathbf{Q},\omega,z,z') = \sum_{G_{z1}G_{z2}} v^{\mathrm{2D}}_{\mathbf{G}_\parallel}(\mathbf{Q},z,G_{z1})\, \chi_{\mathbf{G}_\parallel 0}(\mathbf{Q},\omega,G_{z1},G_{z2}) \times v^{\mathrm{2D}}_0(\mathbf{Q},G_{z2},z'), \tag{10}$$

where

$$v^{2D}_{\mathbf{G}_\parallel}(\mathbf{Q},G_z,z') = \left[v^{2D}_{\mathbf{G}_\parallel}(\mathbf{Q},z,G_z)\right]^* = \int_{-L/2}^{L/2} dz e^{-iG_z z}\, v^{2D}_{\mathbf{G}_\parallel}(\mathbf{Q},z,z')$$

and index zero means that $\mathbf{G}'_\parallel = 0$. If we consider that at $z = a$ the graphene ground-state electronic density vanishes, then for $z,z' > a$ the dynamically screened induced Coulomb interaction can be written as

$$W^{\rm ind}_{\mathbf{G}_\parallel}(\mathbf{Q},\omega,z,z') = e^{-[|\mathbf{Q}+\mathbf{G}_\parallel|z+Qz']} D(\mathbf{Q}+\mathbf{G}_\parallel,\omega), \quad (11)$$

where we have defined the graphene response function

$$D(\mathbf{Q}+\mathbf{G}_\parallel,\omega) = \sum_{G_{z1}G_{z2}} \chi_{G_{z1}G_{z2}}(\mathbf{Q},\omega) F_{G_{z1}}(\mathbf{Q}+\mathbf{G}_\parallel) F^*_{G_{z2}}(\mathbf{Q}) \quad (12)$$

and the form factors $F$ are

$$F_{G_z}(\mathbf{Q}) = p_{G_z} \frac{v_Q}{\sqrt{L}} \frac{1-e^{-QL}}{Q+iG_z}. \quad (13)$$

Equations (11)–(13) provide an important theoretical framework which enables us to study various physical processes near a graphene monolayer. For the response function calculation we have taken the unit cell thickness $L = 23.255$ a.u., which corresponds to five unit cell parameters in the parallel direction. We have neglected crystal local field effects in the parallel but not in the perpendicular direction. By this we mean that, while solving the Dyson equation (6) to obtain the response function, we neglect all $\mathbf{G}_\parallel \neq 0$ components, so it becomes

$$\chi_{G_zG'_z}(\mathbf{Q},\omega) = \chi^0_{G_zG'_z}(\mathbf{Q},\omega) + \sum_{G_{z1}G_{z2}} \chi^0_{G_zG_{z1}}(\mathbf{Q},\omega)\, V_{G_{z1}G_{z2}}(\mathbf{Q}) \times \chi_{G_{z2}G'_z}(\mathbf{Q},\omega). \quad (14)$$

In the Fourier expansion over $G_z$'s we have used the energy cutoff of 20 hartrees, which corresponds to the matrix of dimension $47 \times 47$. This cutoff proved to be sufficient to give a smooth, monotonically decaying tail of induced charge density for $z > a$.

In the next section we use this formulation to calculate the energy loss of the blinking static charge near graphene and the induced potential of the particle moving parallel to the graphene monolayer.

## III. ENERGY LOSS OF A BLINKING POINT CHARGE CLOSE TO THE GRAPHENE MONOLAYER

The energy-loss rate $P(t)$ or the power loss of an arbitrary external dynamical charge distribution $\rho(\mathbf{r},t)$ which induces charge density fluctuations in a polarizable medium can be written in terms of the propagator of induced Coulomb interaction in such a system as

$$P(t) = \int d\mathbf{r}_1 \int d\mathbf{r}_2 \int_{-\infty}^{\infty} \rho(\mathbf{r}_1,t) \frac{\partial}{\partial t} W^{\rm ind}(\mathbf{r}_1,\mathbf{r}_2,t-t_1) \times \rho(\mathbf{r}_2,t_1). \quad (15)$$

The polarizable medium in our case is the graphene monolayer, and the propagator of the induced Coulomb interaction in the real space, expanded in a Fourier series, is

$$W^{\rm ind}(\mathbf{r},\mathbf{r}',t-t') = \sum_{\mathbf{G}_\parallel} \int \frac{d\mathbf{Q}}{(2\pi)^2} e^{i(\mathbf{G}_\parallel+\mathbf{Q})\rho} e^{-i\mathbf{Q}\rho'} \times \int \frac{d\omega}{2\pi} e^{-i\omega(t-t')} W^{\rm ind}_{\mathbf{G}_\parallel}(\mathbf{Q},\omega,z,z'), \quad (16)$$

where Fourier coefficients are given by Eq. (10).

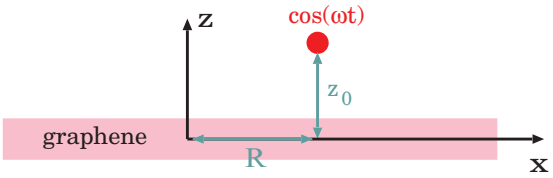


FIG. 4. (Color online) Static blinking point charge placed at position $\mathbf{r}_0 = (\mathbf{R},z_0)$ close to the graphene monolayer.

As a simple example we consider the energy loss of a blinking static point charge, i.e., a point particle placed at $\mathbf{r}_0 = (\mathbf{R},z_0)$, as shown in Fig. 4, with the charge oscillating as

$$\rho(\mathbf{r},t) = \delta(\mathbf{r}-\mathbf{r}_0)\ \cos(\omega t). \quad (17)$$

Then by using Eqs. (15)–(17) the energy-loss rate (or the rate at which the charge loses energy to excitations) becomes[32]

$$P(\omega,\mathbf{r}_0) = -\frac{\omega}{2} \sum_{\mathbf{G}_\parallel} e^{i\mathbf{G}_\parallel \mathbf{R}} \int \frac{d\mathbf{Q}}{(2\pi)^2} {\rm Im} W^{\rm ind}_{\mathbf{G}_\parallel}(\mathbf{Q},\omega,z_0,z_0). \quad (18)$$

Most experiments do not provide information about the spatial variation of the energy-loss rate; e.g., in electron-energy-loss spectroscopy (EELS) experiments the electron passes through or reflects from graphene so the information we obtain is a spatial average value of the energy loss. This means that we can neglect the spatial variation of the energy-loss rate within the unit cell in the parallel direction and it is sufficient to keep only the $\mathbf{G}_\parallel = 0$ Fourier component in Eq. (18). Also, in order to get the loss function with $\mathbf{Q}$ resolution we have to take a single $\mathbf{Q}$ Fourier component, which gives

$$P(\omega,\mathbf{Q},z_0) = -\frac{\omega}{2} {\rm Im} W^{\rm ind}_{\mathbf{G}_\parallel=0}(\mathbf{Q},\omega,z_0,z_0). \quad (19)$$

The advantage of this expression is that it has spatial, frequency, and momentum resolution; i.e., it tells us how much power is lost to the excitation of charge density oscillations at the wave vector $\mathbf{Q}$ and frequency $\omega$, if the driving point charge is placed at a point $z_0$ from the center ($z = 0$) of the graphene monolayer. Using expressions (11) and (12), the induced potential at point $z_0$ can be written in terms of the graphene response function as

$$W^{\rm ind}_{\mathbf{G}_\parallel=0}(\mathbf{Q},\omega,z_0,z_0) = e^{-2Qz_0} D(\mathbf{Q},\omega), \quad (20)$$

where

$$D(\mathbf{Q},\omega) = \sum_{G_{z1}G_{z2}} \chi_{G_{z1}G_{z2}}(\mathbf{Q},\omega) F_{G_{z1}} F^*_{G_{z2}} \quad (21)$$

and the form factors $F$ are given by Eq. (13). As we have previously shown,[33] the dependence of the excitation intensity and frequency on the propagation direction $\mathbf{Q}/Q$ is negligible. Therefore, it is appropriate to calculate the average value of

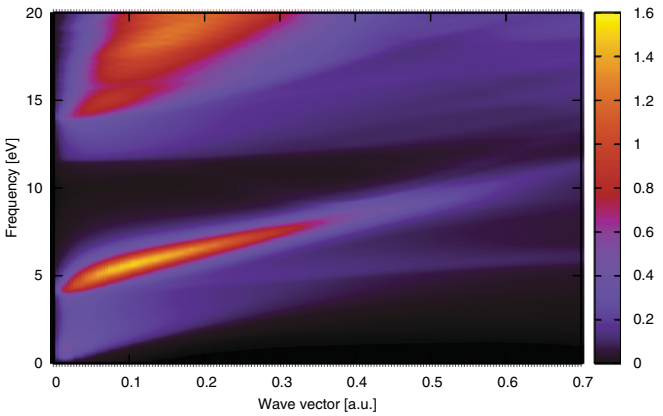


FIG. 5. (Color online) Spectrum of electronic excitations in pristine graphene.

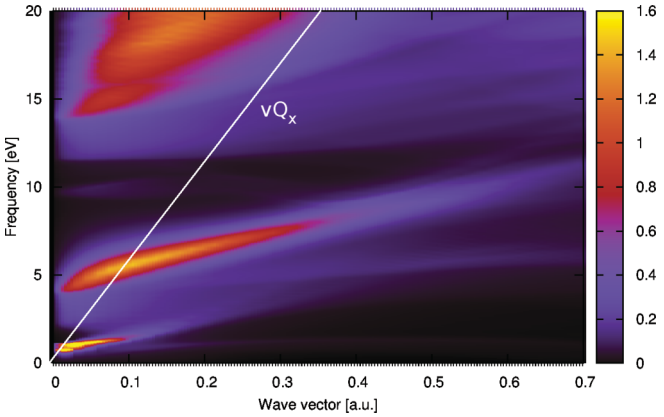


FIG. 6. (Color online) Spectrum of electronic excitations in doped graphene, $E_F = 1$ eV. The white line marks the frequencies and wave vectors of the modes that can be excited by a moving charge at velocity $\mathbf{v} = v\hat{x}$.

$D(\mathbf{Q},\omega)$ over high-symmetry directions. First we calculate $D(\mathbf{Q},\omega)$ for a particular point in the $\Gamma$-$M$ direction, then for the corresponding (so that $|\mathbf{Q}_{\Gamma K}| = |\mathbf{Q}_{\Gamma M}| = Q$) point in the $\Gamma$-$K$ direction, and the average value $D(\mathbf{Q},\omega)$ is then

$$\overline{D}(Q,\omega) = \frac{D(\mathbf{Q}_{\Gamma M},\omega) + D(\mathbf{Q}_{\Gamma K},\omega)}{2}. \tag{22}$$

After substituting Eq. (22) in Eq. (20) and then in Eq. (19), the expression for the average (with respect to the angle of $\mathbf{Q}$) energy-loss rate becomes

$$\overline{P}(\omega,Q,z_0) = -\frac{\omega}{2} e^{-2Qz_0}\,\mathrm{Im}\overline{D}(Q,\omega). \tag{23}$$

This expression can now be used to scan all the graphene electronic modes with respect to frequency and wave vector, which is important for understanding the induced potential which appears behind the moving point charge (as is discussed later). For some distance $z_0$ and wave vector $Q$ the energy-loss rate $\overline{P}$ is proportional to $-\mathrm{Im}\overline{D}(Q,\omega)$, which gives the spectrum of electronic excitations in the graphene monolayer.

Figure 5 shows the spectrum and intensities of electronic excitations in the pristine graphene. Lighter areas indicate frequencies and wave vectors of excitations to which most of the energy can be dissipated. At lower frequencies we can clearly see a wide interband $\pi \to \pi^*$ electron-hole continuum which forms a linearly increasing band about 4 eV wide. On the upper edge of this electron-hole continuum we can see the $\pi$ plasmon with very regular linear dispersion, starting from about 4.3 eV at the $\Gamma$ point. Also we can see the splitting of the $\pi$ plasmon for higher wave vectors, starting from $Q \approx 0.2$ a.u., which is a consequence of $\pi$-plasmon dispersion anisotropy. Namely, as shown before,[33] the $\pi$ plasmon splits only if it propagates in the $\Gamma$-$M$ direction, so here the splitting is a consequence of calculating the average value over high-symmetry directions. At higher frequencies, at about 14 eV at the $\Gamma$ point, we can see a very broad $\pi + \sigma$ plasmon.

We have also used the previous formalism to calculate the excitation spectrum in the doped graphene with the doping parameter $E_F = 1$ eV, which is shown in Fig. 6. We see that doping does not affect the high-energy part of the spectrum, but affects the low-energy excitations. Since now the $\pi^*$ band is partially filled, there is a low-energy $\pi^* \to \pi^*$ intraband electron-hole continuum with low weight, but at its upper edge there is a very strong (very light line starting from $Q = 0$) 2D plasmon.[14] The interband $\pi \to \pi^*$ electron-hole continuum is shifted to higher energies and in between there is a gap which can be seen as a small dark region above the 2D plasmon. Also we see that the 2D plasmon is strong only for very low wave vectors, while at about $Q = 0.1$ a.u. it merges with the lower edge of the $\pi \to \pi^*$ electron-hole continuum and completely disappears.

In the next section we show that all electronic excitations on the $vQ_x$ line shown in Fig. 6 contribute to the potential induced by the particle moving with velocity $v$ parallel to the graphene monolayer. Since the dominant excitations on that line are collective plasmon excitations, we first briefly analyze them analytically.

Since the doping does not influence $\pi$ plasmons, the most general plasmon spectrum can be obtained using the loss data for doped graphene shown in Fig. 6. The plasmon dispersion curves shown in Fig. 7 are obtained by tracking the intensity maxima in the spectrum shown in Fig. 6. In Fig. 7 the $\pi + \sigma$ plasmon is not shown because it is too high in energy and does not contribute to the induced potential. Dispersion curves of plasmons labeled as $\pi_1$ and $\pi_2$ are fitted to linear curves,

$$\omega(Q) = \omega_0 + v_\pi Q, \tag{24}$$

and the 2D plasmon in the long-wavelength limit is fitted to a square root curve

$$\omega(Q) = \omega_0\sqrt{Q}, \tag{25}$$

where $Q$ is in atomic units and fitting parameters are listed in Table I.

As the velocity unit we use the Fermi velocity $v_F$ of a free-electron gas with the density corresponding to $r_s = 3$, which is $v_F = 1.4 \times 10^6$ m/s. The frequency of $\pi$ plasmons at the $\Gamma$ point is in good agreement with the experimental value of 4.7 eV obtained in Refs. 16 and 18. On the other hand, dispersion of the 2D plasmon disagrees with the simple 2D electron gas theory in the long-wavelength limit. Namely, if

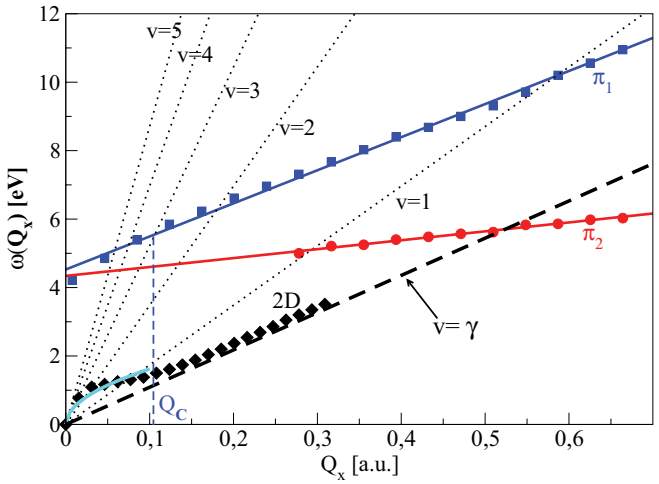


FIG. 7. (Color online) Plasmon dispersion curves in a doped graphene monolayer with $E_F = 1$ eV, obtained by tracking the intensity maxima in Fig. 6, represent $\pi_1$ plasmon (blue squares), $\pi_2$ plasmon (red dots), and 2D plasmon (black diamonds). Solid lines represent the corresponding linear [Eq. (24)] and square root [Eq. (25)] fits. Parameters are listed in Table I. Dotted lines represent $vQ_x$ for $v = 1,2,3,4,5v_F$. The black dashed line represents the upper edge of $\pi^* \to \pi^*$ intraband $e$-$h$ transitions.

electrons in the partially filled $\pi^*$ band (electrons in the Dirac cone) are treated as a 2D electron gas then plasmon dispersion in the long-wavelength limit is given by Eq. (25), where $\omega_0 = \sqrt{2HaE_F}$[14] where $Ha = \frac{e^2}{a_0} = 27.2$ eV. For $E_F = 1$ eV, which is the doping used here, $\omega_0 = 7.37$ eV, which disagrees substantially with the result presented in Table I. We attribute this discrepancy to the fact that this simple 2D theory does not take into account interband $\pi \to \pi^*$ transitions, and also transition matrix elements (2) are not as in the simple 2D theory. Moreover, the 2D plasmon dispersion curve joins the upper edge of $\pi^* \to \pi^*$ intraband $e$-$h$ transitions (shown by black dashed line in Fig. 7) which agrees with the curve presented in Ref. 14 where both interband $\pi \to \pi^*$ $e$-$h$ transitions and tight-binding matrix elements are taken into account.

## IV. STOPPING POWER OF THE MOVING PARTICLE

Previous formulation can be extended to calculate the power loss and the induced potential of a point charge moving with constant velocity **v** parallel to the graphene surface. If a particle moves at height $z_0$ from the graphene center, as shown in Fig. 8, then the external charge density distribution can be written as

$$\rho(\mathbf{r},t) = \delta(x - vt)\delta(y)\delta(z - z_0). \tag{26}$$

TABLE I. 2D and $\pi$-plasmon fitting parameters.

| Plasmon type | $\omega_0$ (eV) | $v_\pi(v_F)$ |
|---|---|---|
| $\pi_1$ | 4.53 | 0.56 |
| $\pi_2$ | 4.34 | 0.15 |
| 2D | 5.13 | |

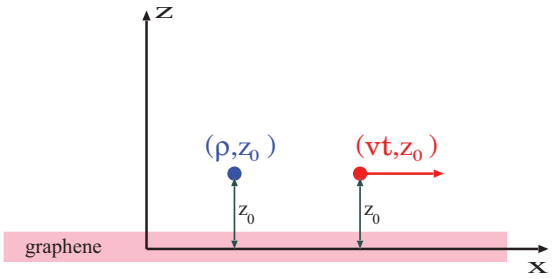


FIG. 8. (Color online) Point charge moving parallel to the graphene monolayer. Red dot shows the current position of moving charge, and blue dot shows the point at which the potential is calculated.

After inserting Eq. (26) into Eq. (15) and using Fourier expansion (16), the power loss becomes

$$P(v,z_0,t) = -i\, v \sum_{\mathbf{G}_\parallel} e^{iG_x vt} \int \frac{d\mathbf{Q}}{(2\pi)^2}\, Q_x\, W^{\rm ind}_{\mathbf{G}_\parallel}(\mathbf{Q},\omega = Q_x v, z_0, z_0). \tag{27}$$

We see that the time dependence of the power loss is periodic, with the time period related to the lattice period in the direction of motion. This could be expected because the particle moves at constant height $z_0$ from the graphene center, so the dissipation power follows surface corrugation. Since such time variations are often very fast, we can calculate the average value of $P(v,z_0,t)$ in the $x = vt$ direction, but we can do the same in the $y$ direction as well, which means that we keep only the $\mathbf{G}_\parallel = 0$ terms in Eq. (27) and it becomes

$$P(v,z_0) = -i\, v \int \frac{d\mathbf{Q}}{(2\pi)^2}\, Q_x\, W^{\rm ind}_{\mathbf{G}_\parallel=0}(\mathbf{Q},\omega = Q_x v, z_0, z_0). \tag{28}$$

Moreover, after using the symmetry properties of the induced potential $W^{\rm ind}$

$$W^{\rm ind}(-Q_x) = [W^{\rm ind}(Q_x)]^*, \quad W^{\rm ind}(-Q_y) = W^{\rm ind}(Q_y)$$

and Eq. (20), which is valid under the assumption that the moving particle is outside the graphene electron density ($z_0 > a$), Eq. (28) can be rewritten as

$$S(v,z_0) = \frac{P(v,z_0)}{v} = \frac{1}{\pi^2}\int_0^\infty dQ_x\, Q_x \int_0^\infty dQ_y\, e^{-2Qz_0} \times {\rm Im}D(\mathbf{Q},\omega = Q_x v), \tag{29}$$

where $S$ represents the force that needs to be applied on the particle to make it move at constant velocity $v$ and is well known as the stopping power.

Figure 9 shows the stopping power for a charged particle moving parallel to the graphene layer as a function of its velocity $v$ and for $z_0 = 10$ a.u. The result for pristine graphene is shown by red dots and the result for doped graphene ($E_F = 1$ eV) is shown by blue squares. As can be seen from Eq. (29), the contributions to stopping power can come from all excitations which lie on the $\omega = Q_x v$ line, schematically shown by the white line in Fig. 6 or by dashed lines (for $v = 1,\ldots,5v_F$) in Fig. 7. In pristine graphene the stopping

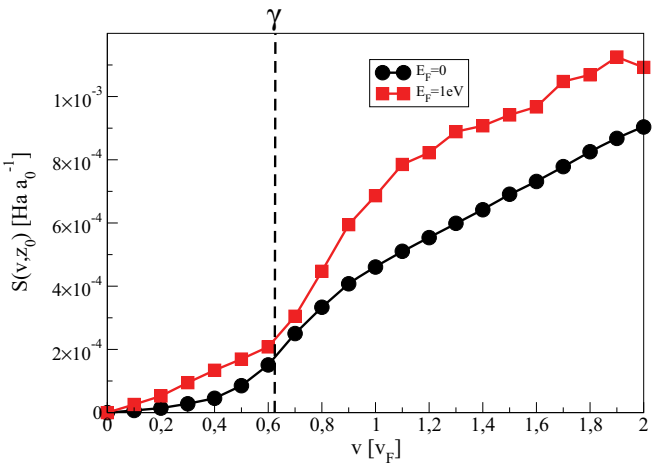


FIG. 9. (Color online) Stopping power $S(v,z_0)$ for particle in parallel motion as a function of its velocity $v$ for pristine (red dots) and doped (blue squares) graphene. Doping parameter is $E_F = 1$ eV and $z_0 = 10$ a.u. The vertical dashed line denotes velocity which corresponds to a graphene cone constant $\gamma = 0.63v_F$.

power first slowly increases (e.g., as $S \sim v^\alpha$, $\alpha \geqslant 2$), then at about $v \approx \gamma$ (where $\gamma$ is the graphene cone constant which in the velocity units we use corresponds to $0.63v_F$, also denoted in Fig. 7) begins to rise more rapidly. This is because the $\omega = vQ_x$ line enters into the region of interband $\pi$-$\pi^*$ electron-hole excitations, whose lower edge is limited by the $\omega = \gamma Q_x$ line, and it becomes the main contribution to particle energy loss. For $v > \gamma$, stopping power has an almost linear trend because then the main contributions come from the excitation of $\pi$ plasmons, which strength linearly increases as $Q_x$ decreases.

For doped graphene the situation is different. For $v < \gamma$ stopping power is above the result for pristine graphene and has a linear character. This is because the $\omega = vQ_x$ line is now below the $\omega = \gamma Q_x$ line which, in doped graphene, represents the upper edge of intraband $\pi^*$-$\pi^*$ electron-hole transitions which are then the dominant contributions to stopping power. For $v > \gamma$, intraband $\pi^*$-$\pi^*$ electron-hole transitions are not contributing any more but stopping power continues to increase with an even bigger slope. This is a consequence of excitation 2D plasmon, which has strong intensity in the gap between intra- and interband continua.

## V. INDUCED OR WAKE POTENTIAL OF THE MOVING PARTICLE

The potential at point $(\boldsymbol{\rho},z_0)$ and at time $t$ induced by an arbitrary external dynamical charge distribution $\rho(\mathbf{r},t)$ can be written in terms of induced Coulomb propagator (10) as[23,24]

$$V(\boldsymbol{\rho},z_0,t) = \int d\mathbf{r}_1 \int_{-\infty}^{\infty} dt_1\, W^{\rm ind}(\boldsymbol{\rho},z_0,\mathbf{r}_1,t-t_1)\rho(\mathbf{r}_1,t_1). \tag{30}$$

Assuming that the external charge is a point charge moving with constant velocity $\mathbf{v}$ parallel to the graphene surface at height $z_0$ from the graphene center, as shown in Fig. 8, then the charge distribution is given by Eq. (26) which after inserting into Eq. (30) gives the induced potential

$$V(\boldsymbol{\rho},z_0,t) = \int_{-\infty}^{\infty} dt_1\, W^{\rm ind}(\boldsymbol{\rho},z_0,\mathbf{v}t_1,z_0,t-t_1). \tag{31}$$

Furthermore, after inserting the Fourier transform of the induced Coulomb propagator

$$\begin{aligned} &W^{\rm ind}(\boldsymbol{\rho},z_0,\mathbf{v}t_1,z_0,t-t_1) \\ &\quad = \sum_{\mathbf{G}_\parallel} e^{i\mathbf{G}_\parallel\boldsymbol{\rho}} \int \frac{d\mathbf{Q}}{(2\pi)^2} e^{i\mathbf{Q}(\boldsymbol{\rho}-\mathbf{v}t_1)} \\ &\qquad \times \int \frac{d\omega}{2\pi} e^{-i\omega(t-t_1)} W^{\rm ind}_{\mathbf{G}_\parallel}(\mathbf{Q},\omega,z_0,z_0), \end{aligned} \tag{32}$$

we can perform $t_1$ integration and the induced potential becomes

$$V(\boldsymbol{\rho},z_0,t) = \sum_{\mathbf{G}_\parallel} e^{i\mathbf{G}_\parallel\boldsymbol{\rho}} \int \frac{d\mathbf{Q}}{(2\pi)^2} e^{i\mathbf{Q}(\boldsymbol{\rho}-\mathbf{v}t)}\, W^{\rm ind}_{\mathbf{G}_\parallel}(\mathbf{Q},\mathbf{Q}\mathbf{v},z_0,z_0). \tag{33}$$

Here we explore the structures in the induced potential with dimensions larger than the unit cell, and then in Eq. (33) it is enough to take just the $\mathbf{G}_\parallel = 0$ component. Also, if we assume that the particle moves in the $\hat{x}$ direction, i.e., $\mathbf{v} = v\hat{x}$, then real (imaginary) parts of $W^{\rm ind}$ become symmetric (antisymmetric) functions of $Q_x$ and symmetric functions of $Q_y$. Then the $\mathbf{Q}$ integration can be explicitly written as

$$\begin{aligned} &V(x-vt,y,z_0) \\ &\quad = \frac{1}{\pi^2}{\rm Re}\int_0^\infty dQ_x e^{iQ_x(x-vt)} \int_0^\infty dQ_y \cos(Q_y y) \\ &\qquad \times W^{\rm ind}_{\mathbf{G}_\parallel=0}(\mathbf{Q},Q_x v,z_0,z_0). \end{aligned} \tag{34}$$

Using Eq. (20), the induced potential also can be written in terms of the graphene response function (22):

$$\begin{aligned} &V(x-vt,y,z_0) \\ &\quad = \frac{1}{\pi^2}{\rm Re}\int_0^\infty dQ_x e^{iQ_x(x-vt)} \int_0^\infty dQ_y \cos(Q_y y)\, e^{-2Qz_0} \\ &\qquad \times D(Q,vQ_x). \end{aligned} \tag{35}$$

This is the final expression we use to calculate the potential induced behind the moving particle. It should be noted here that because of the $x - vt$ dependence in Eq. (35) the induced potential is stationary (time independent) in the reference frame of the moving particle. Watching from the system at rest, we see induced potential moving with velocity $v$ but without changing its shape. From this we can conclude that the moving particle can only excite the modes with phase velocity in the $x$ direction exactly equal to the velocity of the moving particle. In other words, only excitations with phase velocity equal to $v\hat{\mathbf{x}}$ contribute to the induced potential, i.e., all excitations with frequencies $\omega(Q)$ [as can be seen from Eq. (35)] satisfying the relation

$$Q_x v = \omega(Q), \tag{36}$$

where $Q = \sqrt{Q_x^2 + Q_y^2}$. Because of the assumed isotropy the minimal wave vector at which the $vQ_x$ line crosses the particular plasmon dispersion curve has components $Q_x = Q_C$ and $Q_y = 0$. Then for each $Q_x > Q_C$ there will be two

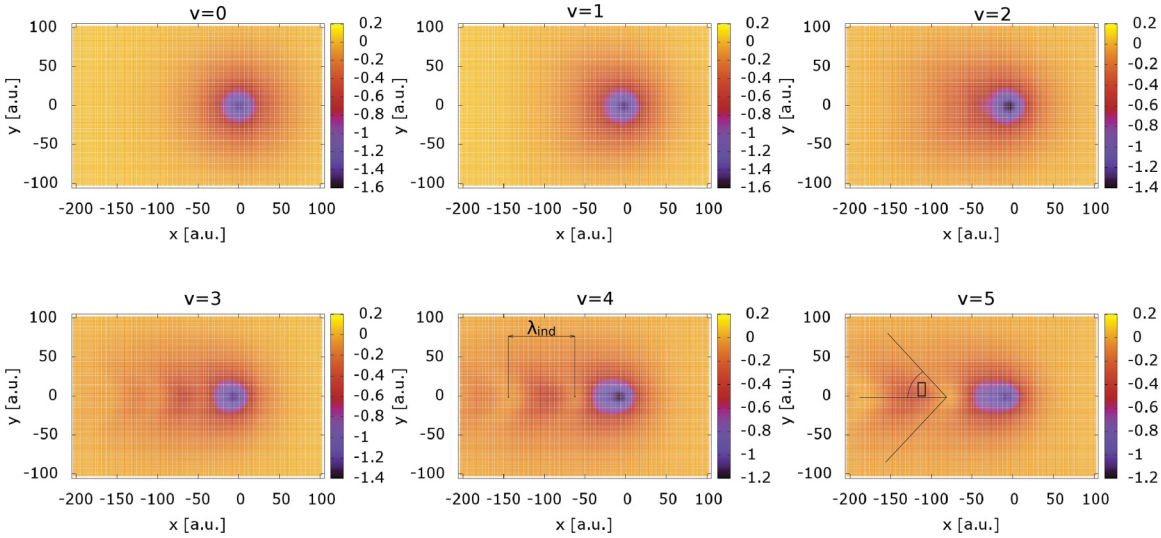


FIG. 10. (Color online) Intensities of the potential induced by point charge moving at distance $z_0 = 10$ a.u. from the center of the pristine graphene monolayer ($E_F = 0$) as functions of coordinates $(x - vt, y)$.

$\pm Q_y$ [according to Eq. (36)] plasmons contributing to the induced potential. However, the contributions of excitations with $Q_y \neq 0$ are weak, and we neglect them. Then the frequencies $\omega$ and wave vectors $Q_x$ of plasmons which dominantly contribute to the induced potential are defined simply as the point where the $vQ_x$ line crosses the plasmon dispersion curve along the $x$ axis:

$$vQ_x = \omega(Q_x). \tag{37}$$

We first analyze the potential induced by the charged particle moving parallel to the pristine graphene monolayer, shown in Fig. 10. Figures show induced potentials at $z_0 = 10$ a.u. as functions of parallel coordinates $(x, y)$ in the reference frame of the moving particle. For $v = 0$, as expected, the induced potential is isotropically distributed around the point charge. It is a standard static screening result, and its detailed analysis as a function of separation $z_0$ and the radial coordinate is presented in Ref. 34. For $v = v_F$ we see a minor deformation, i.e., the sphere is shifted, which is probably due to excitation of $\pi \to \pi^*$ electron-hole transitions lagging behind the particle. In Fig. 7 we see that for $v = v_F$ the line $vQ_x$ crosses the $\pi_1$ and $\pi_2$ plasmon dispersion curves at large $Q_x$ where they are still very weak and do not contribute. For $v = 2v_F$ the sphere is more elongated, which is due to excitations of continuum $\pi \to \pi^*$ interband electron-hole transitions. However, for higher particle velocities $v \geqslant 3v_F$ there is a new feature in the potential which behaves as a wave left behind the moving particle, and we suggest that it originates from excitations of the $\pi_1$ plasmon. This can be checked by comparing the plasmon wavelength

$$\lambda_C = \frac{2\pi}{Q_C}, \tag{38}$$

at which the $vQ_x$ line crosses the $\pi_1$ dispersion curve (an example is shown in Fig. 7) with the wavelength of the induced potential $\lambda_{\text{ind}}$ obtained as a distance between two maxima in the cross section of the induced potential, along the $x$ axis (not shown here). In Table II we compare $\lambda_C$ and $\lambda_{\text{ind}}$ in pristine graphene for velocities $v = 3,4,5v_F$. This nice correlation between the wavelengths confirms that the waves of the induced potential following the particle (Fig. 10 for $v \geqslant 3v_F$) come predominantly from the excitation of the $\pi_1$ plasmon.

Now we examine the behavior of the induced potential in the vicinity of a doped graphene monolayer. Figure 11 shows the potential induced by a charged particle moving at $z_0 = 10$ a.u. from the center of a doped graphene monolayer, where $E_F = 1$ eV. Induced potential is calculated as a function of $x$-$y$ coordinates for $z = z_0$ and in the reference frame of the moving particle. The main difference between the doped and undoped graphene is that doped graphene supports low-energy 2D plasmons, shown by the light line starting from $\omega = 0$ in Fig. 6 or by the black diamonds in Fig. 7. We see that all $Q_x v$ lines cross the 2D plasmon for substantially low $Q_x$'s where the 2D plasmon is still quite strong. Because of that, as we see in Fig. 11, the waves of the induced potential appear already at $v = v_F$, in contrast to the pristine graphene. For higher velocities the $Q_x v$ line crosses the 2D plasmon for lower $Q_x$'s, causing stronger peaks (light areas behind the particles for $v = 2,3v_F$) in the induced potential. As the velocity increases, the first peak increasingly lags behind the particle and, for $v = 3v_F$, comes to the edge of the image. In order to check that for velocities $v = 1,2,3v_F$ the induced potential really comes from 2D plasmons, in Table III we compare the induced potential wavelengths and $\lambda_C = \frac{2\pi}{Q_C}$, where $Q_C$ is now a wave vector

TABLE II. Comparison between $\lambda_C$ for $\pi_1$ plasmon and $\lambda_{\text{ind}}$ shown in Fig. 10 for pristine graphene.

| $v$ ($v_F$) | 3 | 4 | 5 |
|---|---|---|---|
| $\lambda_C$ (a.u.) | 59.2 | 83.2 | 108.3 |
| $\lambda_{\text{ind}}$ ($a.u.$) | 58.6 | 85.1 | 110.1 |

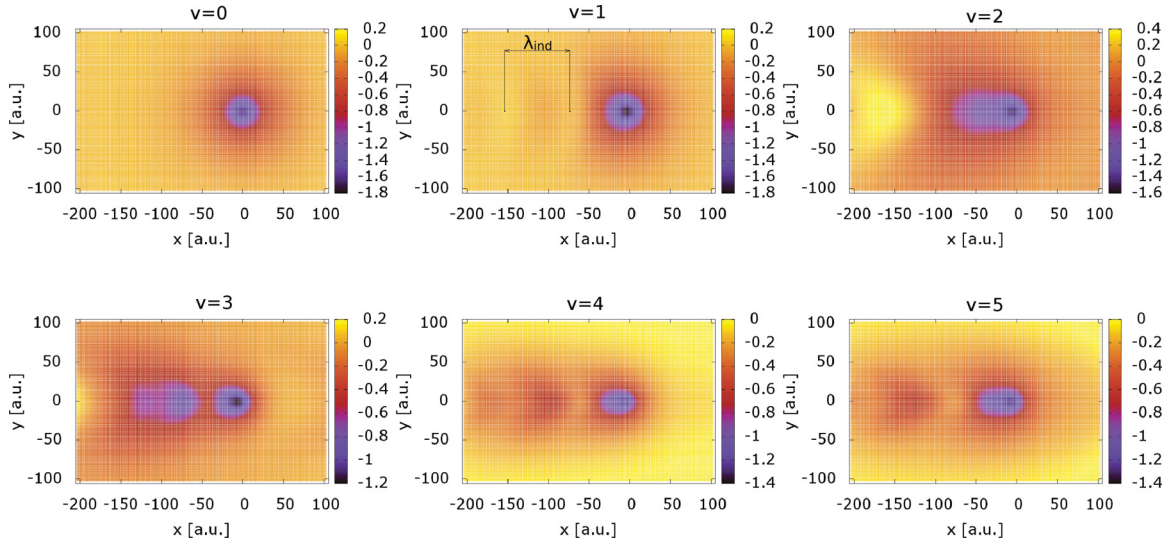


FIG. 11. (Color online) Intensities of the potential induced by point charge moving at distance $z_0 = 10$ a.u. from the center of doped graphene monolayer ($E_F = 1$ eV) as a function of coordinates $(x - vt, y)$.

for which the $Q_x v$ line crosses the 2D plasmon dispersion curve.

We see that the discrepancy increases as velocity increases. This is because for higher velocities the $Q_x v$ line crosses the 2D plasmon dispersion for very small $Q_x$'s, making it very difficult to determine the intersection points exactly. Also, for $v = 3v_F$ convolution with the $\pi_1$ plasmon contribution should be taken into account. However, agreement is good enough to say that the 2D plasmon dominantly deforms the induced potential for lower (up to $3v_F$) velocities. For higher velocities, $v = 4v_F$ and $5v_F$, we see waves appearing in the induced potential similar to those in Fig. 10 for pristine graphene. This could be expected because for higher velocities the $Q_x v$ line does not cross or even touch the 2D plasmon dispersion for very low $Q_x$'s where the density of plasmon states is very low. On the other hand, high-energy $\pi_1$ plasmons which give the dominant contribution to the induced potential are unaffected by doping.

In Fig. 10 we marked the wave front of the induced potential to show that the wave propagates in the direction corresponding to the wave vector $\mathbf{Q} = Q_C(1, ctg\theta)$; i.e., the propagation in not parallel to the $x$ axis. The reason for this is the retardation effect in the propagation of the Coulomb interaction, i.e., retardation in the plasmon formation (which gives the main contribution in this case). The plasmon creation is not instantaneous, which means that at the time when the particle excites the plasmon at some position, the plasmon earlier created at some of the particle's previous positions has already moved in the $y$ direction. Since the phase velocity of such creation remains exactly $v$, this causes inclination of the wave front from the direction of propagation, by an angle $\theta = \frac{\pi}{4}$, as shown in Fig. 10.

TABLE III. Comparison between $\lambda_C$ for 2D plasmon and $\lambda_{\text{ind}}$ shown in Fig. 11 for doped graphene.

| $v$ ($v_F$) | 1 | 2 | 3 |
|---|---|---|---|
| $\lambda_C$ (a.u.) | 85 | 273 | 570 |
| $\lambda_{\text{ind}}$ (a.u.) | 87 | 252 | 373 |

## VI. CONCLUSION

This paper demonstrates, in a clear formal way, the usefulness of the nonlocal dynamical Coulomb interaction in theoretical investigation of graphene response to arbitrary external longitudinal perturbation. To test this approach we used the simplest longitudinal probes, blinking stationary point charge and a moving point charge. We calculated the energy-loss rate of a point blinking charge in the vicinity of graphene from the imaginary part of nonlocal dynamical Coulomb interaction. By scanning the energy dissipation across all $(Q,\omega)$ space we obtained the map of collective and single-particle excitations in pristine and doped graphene, with energies in very good agreement with previous experimental and theoretical results. We use the imaginary part of the dynamically screened Coulomb interaction to calculate stopping power, and we used its real part to calculate the induced potential caused by a point charge moving parallel to the graphene monolayer. We showed that for velocities up to $v \approx 3v_F$ the dominant contribution to the induced potential bow waves occurring behind the moving charge comes from excitations of a 2D or Drude plasmon existing only in doped graphene. On the other hand, for higher velocities $v > 3v_F$ the dominant contribution to induced potential bow waves comes from excitation of $\pi_1$ plasmons.

## ACKNOWLEDGMENTS

Two of the authors (V.D. and M.Š.) are grateful to Donostia International Physics Center (DIPC) and Pedro M. Echenique for the hospitality during various stages of this research. We also thank D. J. Mowbray and V. Silkin for useful discussions.

*vito@phy.hr
†kdekanic@phy.hr
‡msunjic@phy.hr
§lmarusic@unizd.hr

[1]K. S. Novoselov *et al.*, Nature (London) **438**, 197 (2005).
[2]Y. Zhang, Y. W. Tan, H. L. Stormer, and P. Kim, Nature (London) **438**, 201 (2005).
[3]K. S. Novoselov, A. K. Geim, S. V. Morozov, D. Jiang, Y. Zhang, S. V. Dubonos, I. V. Grigorieva, and A. A. Firsov, Science **306**, 666 (2004).
[4]K. S. Novoselov, D. Jiang, F. Schedin, T. J. Booth, V. V. Khotkevich, S. V. Morozov, and A. K. Geim, Proc. Natl. Acad. Sci. USA **102**, 10451 (2005).
[5]K. S. Novoselov, A. K. Geim, S. V. Morozov, D. Jiang, M. I. Katsnelson, I. V. Grigorieva, S. V. Dubonos, and A. A. Firsov, Nature (London) **438**, 197 (2005).
[6]A. K. Geim and K. S. Novoselov, Nat. Mater. **6**, 183 (2007).
[7]I. Pletikosić, M. Kralj, P. Pervan, R. Brako, J. Coraux, A. T. N'Diaye, C. Busse, and T. Michely, Phys. Rev. Lett. **102**, 056808 (2009).
[8]F. Bonaccorso, Z. Sun, T. Hasan, and A. C. Ferrari, Nat. Photonics **4**, 611 (2010).
[9]M. Jablan, H. Buljan, and M. Soljačić, Phys. Rev. B **80**, 245435 (2009).
[10]Frank H. L. Koppens, Darrick E. Chang, and F. Javier Garcia de Abajo, Nano Lett. **11**, 3370 (2011).
[11]Y. Zhang, Tsung-Ta Tang, C. Girit, Z. Hao, Michael C. Martin, A. Zettl, Michael F. Crommie, and Y. Ron Shen Feng Wang, Nature **459**, 820 (2009).
[12]Sung Won Hwang, Dong Hee Shin, Chang Oh Kim, Seung Hui Hong, Min Choul Kim, Jungkil Kim, Keun Yong Lim, Sung Kim, Suk-Ho Choi, Kwang Jun Ahn, Gunn Kim, Sung Hyun Sim, and Byung Hee Hong, Phys. Rev. Lett. **105**, 127403 (2010).
[13]B. N. J. Persson and H. Ueba, J. Phys.: Condens. Matter **22**, 462201 (2010).
[14]E. H. Hwang and S. Das Sarma, Phys. Rev. B **75**, 205418 (2007); **80**, 205405 (2009).
[15]Yi Gao and Z. Yuan, Solid State Commun. **151**, 1009 (2011).
[16]T. Eberlein, U. Bangert, R. R. Nair, R. Jones, M. Gass, A. L. Bleloch, K. S. Novoselov, A. Geim, and P. R. Briddon, Phys. Rev. B **77**, 233406 (2008).
[17]C. Tegenkamp, H. Pfnur, T. Langer, J. Baringhaus, and H. W. Schumacher, J. Phys.: Condens. Matter **23**, 012001 (2011).
[18]J. Lu, K. P. Loh, H. Huang, W. Chen, and Andrew T. S. Wee, Phys. Rev. B **80**, 113410 (2009).
[19]C. Kramberger, F. Roth, R. Schuster, R. Kraus, M. Knupfer, E. Einarsson, S. Maruyama, D. J. Mowbray, A. Rubio, and T. Pichler, Phys. Rev. B **85**, 085424 (2012).
[20]I. Radović, D. Borka, and Zoran L. Mišković, Phys. Lett. A **375**, 3720 (2011).
[21]D. J. Mowbray, Z. L. Mišković, F. O. Goodman, and You-Nian Wang, Phys. Lett. A **329**, 94 (2004).
[22]R. Nunez, P. M. Echenique, and R. H. Ritchie, J. Phys. C **13**, 4229 (1980).
[23]F. J. Garcia de Abajo and P. M. Echenique, Phys. Rev. B **46**, 2663 (1992).
[24]F. J. Garcia de Abajo and P. M. Echenique, Phys. Rev. B **48**, 13399 (1993).
[25]R. H. Ritchie and A. L. Marusak, Surf. Sci. **4**, 234 (1966).
[26]V. B. Jovanović, I. Radović, D. Borka, and Z. L. Mišković, Phys. Rev. B **84**, 155416 (2011).
[27]C. Kramberger, R. Hambach, C. Giorgetti, M. H. Rummeli, M. Knupfer, J. Fink, B. Buchner, Lucia Reining, E. Einarsson, S. Maruyama, F. Sottile, K. Hannewald, V. Olevano, A. G. Marinopoulos, and T. Pichler, Phys. Rev. Lett. **100**, 196803 (2008).
[28]P. Giannozzi, S. Baroni, N. Bonini, M. Calandra, R. Car, C. Cavazzoni, D. Ceresoli, G. L. Chiarotti, M. Cococcioni, I. Dabo *et al.*, J. Phys.: Condens. Matter **21**, 395502 (2009).
[29]J. P. Perdew and A. Zunger, Phys. Rev. B **23**, 5048 (1981).
[30]N. Troullier and J. L. Martins, Phys. Rev. B **43**, 1993 (1991).
[31]P. E. Trevisanutto, C. Giorgetti, L. Reining, M. Ladisa, and V. Olevano, Phys. Rev. Lett. **101**, 226405 (2008); C. Attaccalite, A. Grüeneis, T. Pichler, and A. Rubio, arXiv:0808.0786v2.
[32]L. Marušić and M. Šunjić, Phys. Scr. **63**, 336 (2001).
[33]D. J. Mowbray, V. Despoja, P. Ayala, T. Pichler, and A. Rubio (unpublished).
[34]V. Despoja, D. J. Mowbray, D. Vlahović, and L. Marušić (unpublished).